interesting circuit capabilities. The thin polymer interlayers allow robust interconnects to be formed easily by evaporating metal lines over lithographically defined openings. Thermal cycling tests showed no changes in their properties (fig. S10). Figure 4A shows a 3D n-channel metal oxide semiconductor inverter (logic gate) in which the drive (L = 4 μm, W = 200 μm) and load (L = 4 μm, W = 30 μm) Si MOSFETs are on different levels. With a supply voltage of 5 V, this double-layer inverter exhibits well-defined transfer characteristics with gains of ~2, comparable to the performance of conventional planar inverters that use similar transistors. Figure 4B shows an inverter with a complementary design (CMOS) with the use of integrated n-channel Si MOSFETs and p-channel SWNT TFTs, designed to equalize the current-driving capability in both pull-up and pull-down directions. Transfer curves collected with a supply voltage (V_{DD}) of 5 V and gate voltage (input) swept from 0 to 5 V appear in Fig. 4B. The curve shapes and gains (as high as ~7) are qualitatively consistent with numerical circuit simulations (fig. S6). As a third example, we built GaAs metal-semiconductor-metal (MSM) infrared detectors (*26*), integrated with Si MOSFETs on flexible PI substrates, to demonstrate a capability for fabricating unit cells that could be used in active infrared imagers. In this case, printed nanoribbons of GaAs (L = 400 μm, W = 100 μm, and thickness = 270 nm) transferred onto a substrate with a printed array of Si nanoribbon MOSFETs form the basis of the MSMs. Electrodes (Ti/Au) deposited on the ends of these GaAs nanoribbons form back-to-back Schottky diodes with separations of 10 μm. The resulting detector cells exhibit current enhancement as the intensity of infrared illumination increases (Fig. 4C), consistent with circuit simulation (fig. S7). A responsivity of about 0.30 A/W at the 850-nm wavelength is observed from 1 to 5 V. (This value underestimates the true responsivity because it ignores optical reflection). The bendability of this system, which is comparable to that of the devices in Fig. 3, could be useful for advanced systems such as curved focal plane arrays for wide-angle infrared night vision imagers.

Printed semiconductor nanomaterials provide new approaches to 3D heterogeneously integrated systems that could be important in various fields of application, including not only those suggested by the systems reported here but also others such as microfluidic devices with integrated electronics, chemical and biological sensor systems that incorporate unusual materials with conventional silicon-based electronics, and photonic and optoelectronic systems that combine light emitters and detectors of compound semiconductor with silicon drive electronics or microelectromechanical structures. Furthermore, the compatibility of this approach with thin, lightweight plastic substrates may create additional opportunities for devices that have unusual form factors or mechanical flexibility as key features.

References and Notes

1. K. Banerjee, S. J. Souri, P. Kapur, K. C. Saraswat, *Proc. IEEE* **89**, 602 (2001).
2. S. F. Al-Sarawi, D. Abbott, P. D. Franzon, *IEEE Trans. Components Packaging Manufacturing Technol. Part B* **21**, 2 (1998).
3. A. S. Brown *et al.*, *Mater. Sci. Eng. B* **87**, 317 (2001).
4. Y.-C. Tseng *et al.*, *Nano Lett.* **4**, 123 (2004).
5. C. Joachim, J. K. Gimzewski, A. Aviram, *Nature* **408**, 541 (2000).
6. G. Roelkens *et al.*, *Opt. Express* **13**, 10102 (2005).
7. D. B. Strukov, K. K. Likharev, *Nanotechnology* **16**, 888 (2005).
8. Q. Y. Tong, U. Gosele, *Semiconductor Wafer Bonding: Science and Technology* (John Wiley, New York, 1999).
9. M. A. Schmidt, *Proc. IEEE* **86**, 1575 (1998).
10. P. Garrou, *Semicond. Int.* **28**, SP10 (February, 2005).
11. H. Amano, N. Sawaki, I. Akasaki, Y. Toyoda, *Appl. Phys. Lett.* **48**, 353 (1986).
12. T. Kuykendall *et al.*, *Nat. Mater.* **3**, 524 (2004).
13. J. C. Bean, *Proc. IEEE* **80**, 571 (1992).
14. A. M. Morales, C. M. Lieber, *Science* **279**, 208 (1998).
15. M. Law *et al.*, *Science* **305**, 1269 (2004).
16. J. Kong, H. T. Soh, A. M. Cassell, C. F. Quate, H. Dai, *Nature* **395**, 878 (1998).
17. K. S. Novoselov *et al.*, *Science* **306**, 666 (2004).
18. Y. Huang, X. Duan, C. M. Lieber, *Small* **1**, 142 (2005).
19. M. A. Meitl *et al.*, *Nat. Mater.* **5**, 33 (2006).
20. E. Menard, K. J. Lee, D. Y. Khang, R. G. Nuzzo, J. A. Rogers, *Appl. Phys. Lett.* **84**, 5398 (2004).
21. Y. Sun, S. Kim, I. Adesida, J. A. Rogers, *Appl. Phys. Lett.* **87**, 083501 (2005).
22. S.-H. Hur, D.-Y. Khang, C. Kocabas, J. A. Rogers, *Appl. Phys. Lett.* **85**, 5730 (2004).
23. Materials and methods are available as supporting material on *Science* Online.
24. S. Linder, H. Baltes, F. Gnaedinger, E. Doering, in *Proceedings of the 7th IEEE International Workshop on Micro Electro Mechanical Systems*, Oiso, Japan, 25 to 28 January 1994 (IEEE, Piscataway, NJ, 1994), pp. 349–354.
25. J.-H. Ahn *et al.*, *IEEE Electron Devices Lett* **27**, 460 (2006).
26. J. B. D. Soole, H. Schumacher, *IEEE J. Quantum Electron.* **27**, 737 (1991).

27. The research was supported by the U.S. Department of Energy, Division of Materials Sciences under award no. DEFG02-91ER45439, through the Frederick Seitz Materials Research Laboratory (FS-MRL). We thank T. Banks and K. Colravy for help with cleanroom and other facilities at the Frederick Seitz Materials Research Laboratory and H. C. Ko, Q. Cao, P. Ferreira, J. Dong, and E. Menard for help with printing and distortion measurements using facilities and manufacturing approaches developed at the Center for Nanoscale Chemical Electrical Mechanical Manufacturing Systems at the University of Illinois (funded by the NSF under grant DMI-0328162). All imaging and surface analysis was performed at the FS-MRL Center for Microanalysis of Materials at the University of Illinois at Urbana-Champaign, supported by award no. DEFG02-91ER45439.

Supporting Online Material

www.sciencemag.org/cgi/content/full/314/5806/1754/DC1
Materials and Methods
Figs. S1 to S15

12 July 2006; accepted 31 October 2006
10.1126/science.1132394

Quantum Spin Hall Effect and Topological Phase Transition in HgTe Quantum Wells

B. Andrei Bernevig,[1,2] Taylor L. Hughes,[1] Shou-Cheng Zhang[1]*

We show that the quantum spin Hall (QSH) effect, a state of matter with topological properties distinct from those of conventional insulators, can be realized in mercury telluride–cadmium telluride semiconductor quantum wells. When the thickness of the quantum well is varied, the electronic state changes from a normal to an "inverted" type at a critical thickness d_c. We show that this transition is a topological quantum phase transition between a conventional insulating phase and a phase exhibiting the QSH effect with a single pair of helical edge states. We also discuss methods for experimental detection of the QSH effect.

The spin Hall effect (*1*–*5*) has recently attracted great attention in condensed matter physics, not only for its fundamental scientific importance but also because of its potential application in semiconductor spintronics. In particular, the intrinsic spin Hall effect promises the possibility of designing the intrinsic electronic properties of materials so that the effect can be maximized. On the basis of this line of reasoning, it was shown (*6*) that the intrinsic spin Hall effect can in principle exist in band insulators, where the spin current can flow without dissipation. Motivated by this suggestion, researchers have proposed the quantum spin Hall (QSH) effect for graphene (*7*) as well as for semiconductors (*8*, *9*), where the spin current is carried entirely by the helical edge states in two-dimensional samples.

Time-reversal symmetry plays an important role in the dynamics of the helical edge states (*10*–*12*). When there is an even number of pairs of helical states at each edge, impurity scattering or many-body interactions can open a gap at the edge and render the system topologically trivial. However, when there is an odd number of pairs of helical states at each edge, these effects cannot open a gap unless time-reversal symmetry is

[1]Department of Physics, Stanford University, Stanford, CA 94305, USA. [2]Kavli Institute for Theoretical Physics, University of California, Santa Barbara, CA 93106, USA.

*To whom correspondence should be addressed. E-mail: sczhang@stanford.edu

spontaneously broken at the edge. The stability of the helical edge states has been confirmed in extensive numerical calculations (*13*, *14*). The time-reversal property leads to the Z_2 classification (*10*) of the QSH state.

States of matter can be classified according to their topological properties. For example, the integer quantum Hall effect is characterized by a topological integer n (*15*), which determines the quantized value of the Hall conductance and the number of chiral edge states. It is invariant under smooth distortions of the Hamiltonian, as long as the energy gap does not collapse. Similarly, the number of helical edge states, defined modulo 2, of the QSH state is also invariant under topologically smooth distortions of the Hamiltonian. Therefore, the QSH state is a topologically distinct new state of matter, in the same sense as the charge quantum Hall effect.

Unfortunately, the initial proposal of the QSH in graphene (*7*) was later shown to be unrealistic (*16*, *17*), as the gap opened by the spin-orbit interaction turns out to be extremely small, on the order of 10^{-3} meV. There are also no immediate experimental systems available for the proposals in (*8*, *18*). Here, we present theoretical investigations of the type III semiconductor quantum wells, and we show that the QSH state should be realized in the "inverted" regime where the well thickness d is greater than a certain critical thickness d_c. On the basis of general symmetry considerations and the standard band perturbation theory for semiconductors, also called $k \cdot p$ theory (*19*), we show that the electronic states near the Γ point are described by the relativistic Dirac equation in 2 + 1 dimensions. At the quantum phase transition at $d = d_c$, the mass term in the Dirac equation changes sign, leading to two distinct $U(1)$-spin and Z_2 topological numbers on either side of the transition. Generally, knowledge of electronic states near one point of the Brillouin zone is insufficient to determine the topology of the entire system; however, it does allow robust and reliable predictions on the change of topological quantum numbers. The fortunate presence of a gap-closing transition in the HgTe-CdTe quantum wells therefore makes our theoretical prediction of the QSH state conclusive.

The potential importance of inverted band-gap semiconductors such as HgTe for the spin Hall effect was pointed out in (*6*, *9*). The central feature of the type III quantum wells is band inversion: The barrier material (e.g., CdTe) has a normal band progression, with the s-type Γ_6 band lying above the p-type Γ_8 band, and the well material (HgTe) having an inverted band progression whereby the Γ_6 band lies below the Γ_8 band. In both of these materials, the gap is smallest near the Γ point in the Brillouin zone (Fig. 1). In our discussion we neglect the bulk split-off Γ_7 band, as it has negligible effects on the band structure (*20*, *21*). Therefore, we restrict ourselves to a six-band model, and we start with the following six basic atomic states per unit cell combined into a six-component spinor:

$$\Psi = \left(|\Gamma_6, {}^1/_2\rangle, |\Gamma_6, {}^{-1}/_2\rangle, |\Gamma_8, {}^3/_2\rangle, |\Gamma_8, {}^1/_2\rangle, |\Gamma_8, {}^{-1}/_2\rangle, |\Gamma_8, {}^{-3}/_2\rangle\right) \quad (1)$$

In quantum wells grown in the [001] direction, the cubic or spherical symmetry is broken down to the axial rotation symmetry in the plane. These six bands combine to form the spin-up and spin-down (±) states of three quantum well subbands: $E1$, $H1$, and $L1$ (*21*). The $L1$ subband is separated from the other two (*21*), and we neglect it, leaving an effective four-band model. At the Γ point with in-plane momentum $k_{\|} = 0$, m_J is still a good quantum number. At this point the $|E1, m_J\rangle$ quantum well subband state is formed from the linear combination of the $|\Gamma_6, m_J = \pm{}^1/_2\rangle$ and $|\Gamma_8, m_J = \pm{}^1/_2\rangle$ states, while the $|H1, m_J\rangle$ quantum well subband state is formed from the $|\Gamma_8, m_J = \pm{}^3/_2\rangle$ states. Away from the Γ point, the $E1$ and $H1$ states can mix. Because the $|\Gamma_6, m_J = \pm{}^1/_2\rangle$ state has even parity, whereas the $|\Gamma_8, m_J = \pm{}^3/_2\rangle$ state has odd parity under two-dimensional spatial reflection, the coupling matrix element between these two states must be an odd function of the in-plane momentum k. From these symmetry considerations, we deduce the general form of the effective Hamiltonian for the $E1$ and $H1$ states, expressed in the basis of $|E1, m_J = {}^1/_2\rangle$, $|H1, m_J = {}^3/_2\rangle$ and $|E1, m_J = -{}^1/_2\rangle$, $|H1, m_J = -{}^3/_2\rangle$:

$$H_{\text{eff}}(k_x, k_y) = \begin{pmatrix} H(k) & 0 \\ 0 & H^*(-k) \end{pmatrix}, \quad H(k) = \varepsilon(k) + d_i(k)\sigma_i \quad (2)$$

where σ_i are the Pauli matrices. The form of $H^*(-k)$ in the lower block is determined from time-reversal symmetry, and $H^*(-k)$ is unitarily equivalent to $H^*(k)$ for this system (*22*). If inversion symmetry and axial symmetry around the growth axis are not broken, then the interblock matrix elements vanish, as presented.

We see that, to the lowest order in k, the Hamiltonian matrix decomposes into 2 × 2 blocks. From the symmetry arguments given above, we deduce that $d_3(k)$ is an even function of k, whereas $d_1(k)$ and $d_2(k)$ are odd functions of k. Therefore, we can generally expand them in the following form:

$$d_1 + id_2 = A(k_x + ik_y) \equiv Ak_+$$

$$d_3 = M - B(k_x^2 + k_y^2), \ \varepsilon(k) = C - D(k_x^2 + k_y^2) \quad (3)$$

where A, B, C, and D are expansion parameters that depend on the heterostructure. The Hamiltonian in the 2 × 2 subspace therefore takes the form of the (2 + 1)-dimensional Dirac Hamiltonian, plus an $\varepsilon(k)$ term that drops out in the quantum Hall response. The most important quantity is the mass or gap parameter M, which is the energy difference between the $E1$ and $H1$ levels at the Γ point. The overall constant C sets the zero of energy to be the top of the valence band of bulk HgTe. In a quantum well geometry, the band inversion in HgTe necessarily leads to a level crossing at some critical thickness d_c of the HgTe layer. For thickness $d < d_c$ (i.e., for a thin HgTe

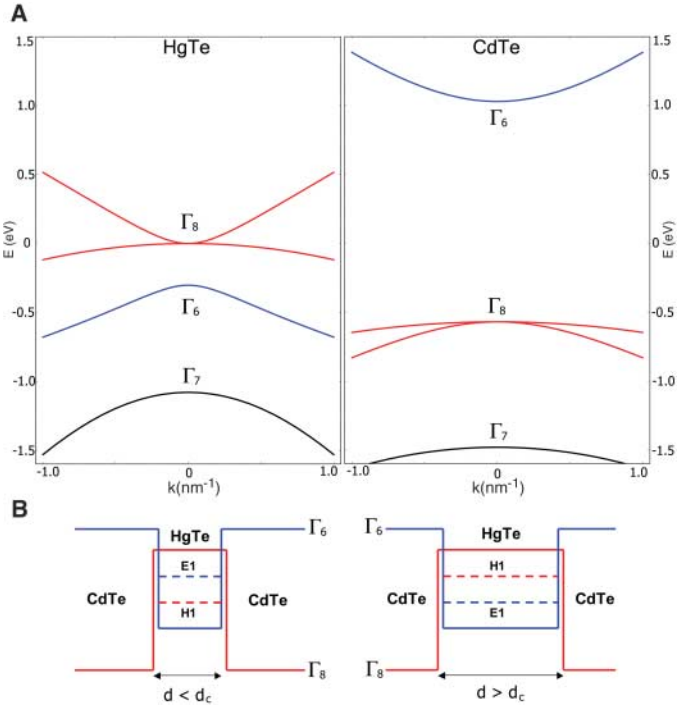

Fig. 1. (**A**) Bulk energy bands of HgTe and CdTe near the Γ point. (**B**) The CdTe-HgTe-CdTe quantum well in the normal regime $E1 > H1$ with $d < d_c$ and in the inverted regime $H1 > E1$ with $d > d_c$. In this and other figures, $\Gamma_8/H1$ symmetry is indicated in red and $\Gamma_6/E1$ symmetry is indicated in blue.

layer), the quantum well is in the "normal" regime, where the CdTe is predominant and hence the band energies at the Γ point satisfy $E(\Gamma_6) > E(\Gamma_8)$. For $d > d_c$, the HgTe layer is thick and the well is in the inverted regime, where HgTe dominates and $E(\Gamma_6) < E(\Gamma_8)$. As we vary the thickness of the well, the $E1$ and $H1$ bands must therefore cross at some d_c, and M changes sign between the two sides of the transition (Fig. 2, A and B). Detailed calculations show that, close to transition point, the $E1$ and $H1$ bands—both doubly degenerate in their spin quantum number—are far away in energy from any other bands (*21*), hence making an effective Hamiltonian description possible. Indeed, the form of the effective Dirac Hamiltonian and the sign change of M at $d = d_c$ for the HgTe-CdTe quantum wells deduced above from general arguments is already completely sufficient to conclude the existence of the QSH state in this system. For the sake of completeness, we also provide the microscopic derivation directly from the Kane model using realistic material parameters (*22*).

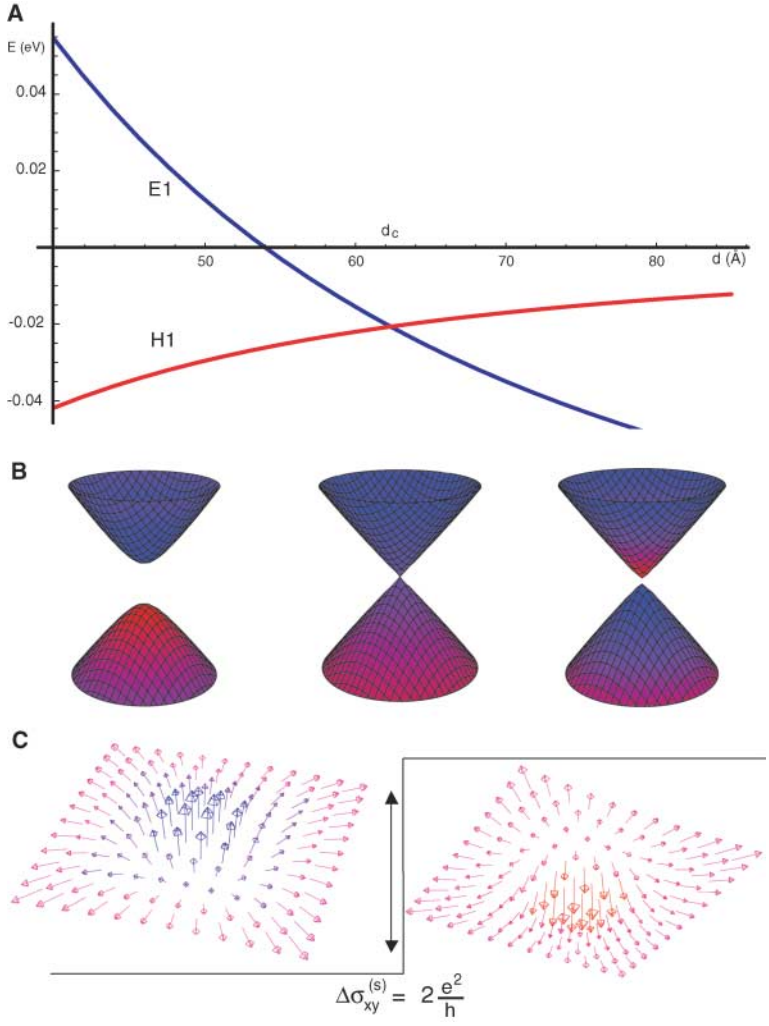

Fig. 2. (**A**) Energy of $E1$ (blue) and $H1$ (red) bands at $k_{||} = 0$ versus quantum well thickness d. (**B**) Energy dispersion relations $E(k_x,k_y)$ of the $E1$ and $H1$ subbands at $d = 40$, 63.5, and 70 Å (from left to right). Colored shading indicates the symmetry type of the band at that k point. Places where the cones are more red indicate that the dominant state is $H1$ at that point; places where they are more blue indicate that the dominant state is $E1$. Purple shading is a region where the states are more evenly mixed. At 40 Å, the lower band is dominantly $H1$ and the upper band is dominantly $E1$. At 63.5 Å, the bands are evenly mixed near the band crossing and retain their $d < d_c$ behavior moving farther out in k-space. At 70 Å, the regions near $k_{||} = 0$ have flipped their character but eventually revert back to the $d < d_c$ farther out in k-space. Only this dispersion shows the meron structure (red and blue in the same band). (**C**) Schematic meron configurations representing the $d_i(k)$ vector near the Γ point. The shading of the merons has the same meaning as the dispersion relations above. The change in meron number across the transition is exactly equal to 1, leading to a quantum jump of the spin Hall conductance $\sigma_{xy}^{(s)} = 2e^2/h$. We measure all Hall conductances in electrical units. All of these plots are for $Hg_{0.32}Cd_{0.68}Te$-HgTe quantum wells.

Figure 2A shows the energies of both the $E1$ and $H1$ bands at $k_{||} = 0$ as a function of quantum well thickness d obtained from our analytical solutions. At $d = d_c \sim 64$ Å, these bands cross. Our analytic results are in excellent qualitative and quantitative agreement with previous numerical calculations for the band structure of $Hg_{1-x}Cd_xTe$-HgTe-$Hg_{1-x}Cd_xTe$ quantum wells (*20*, *21*). We also observe that for quantum wells of thickness 40 Å $< d <$ 70 Å, close to d_c, the $E1\pm$ and $H1\pm$ bands are separated from all other bands by more than 30 meV (*21*).

Let us now define an ordered set of four six-component basis vectors $\psi_{1,\ldots,4} = (|E1, +\rangle, |H1, +\rangle, |E1, -\rangle, |H1, -\rangle)$ and obtain the Hamiltonian at nonzero in-plane momentum in perturbation theory. We can write the effective 4 × 4 Hamiltonian for the $E1\pm$, $H1\pm$ bands as

$$H_{ij}^{\text{eff}}(k_x, k_y) = \int_{-\infty}^{\infty} dz \langle \psi_j | \mathcal{H}(k_x, k_y, -i\partial_z) | \psi_i \rangle \tag{4}$$

where $\mathcal{H}(k_x, k_y, -i\partial_z)$ is the six-band Kane model (*19*). The form of the effective Hamiltonian is severely constrained by symmetry with respect to z. Each band has a definite z symmetry or antisymmetry, and vanishing matrix elements between them can be easily identified. For example,

$$H_{23}^{\text{eff}} = \frac{1}{\sqrt{6}} P k_+ \int_{-\infty}^{\infty} dz \langle \Gamma_6, +1/2(z) | \Gamma_8, -1/2(z) \rangle \tag{5}$$

where P is the Kane matrix element (*19*), vanishes because $|\Gamma_6, +1/2\rangle(z)$ is even in z, whereas $|\Gamma_8, -1/2\rangle(z)$ is odd. The procedure yields exactly the form of the effective Hamiltonian (Eq. 2), as we anticipated from the general symmetry arguments, with the coupling functions taking exactly the form of Eq. 3. The dispersion relations (*22*) have been checked to be in agreement with prior numerical results (*20*, *21*). We note that for $k \in [0, 0.01\ \text{Å}^{-1}]$ the dispersion relation is dominated by the Dirac linear terms. The numerical values for the coefficients depend on the thickness, and values at $d = 58$ Å and $d =$ 70 Å are given in (*22*).

Having presented the realistic $k \cdot p$ calculation starting from the microscopic six-band Kane model, we now introduce a simplified tight-binding model for the $E1$ and $H1$ states based on their symmetry properties. We consider a square lattice with four states per unit cell. The $E1$ states are described by the s-orbital states $\psi_{1,3} = |s,\alpha = \pm 1/2\rangle$, and the $H1$ states are described by the spin-orbit coupled p-orbital states $\psi_{2,4} = \pm(1/\sqrt{2})|p_x \pm ip_y, \alpha = \pm 1/2\rangle$, where α denotes the electron spin. Nearest-neighbor coupling between these states gives the tight-

binding Hamiltonian of the form of Eq. 2, with the matrix elements given by

$$d_1 + id_2 = A[\sin(k_x) + i\,\sin(k_y)]$$

$$d_3 = -2B[2 - (M/2B) - \cos(k_x) - \cos(k_y)]$$

$$\varepsilon(k) = C - 2D[2 - \cos(k_x) - \cos(k_y)] \quad (6)$$

The tight-binding lattice model simply reduces to the continuum model Eq. 2 when expanded around the Γ point. The tight-binding calculation serves dual purposes. For readers uninitiated in the Kane model and $k \cdot p$ theory, this gives a simple and intuitive derivation of our effective Hamiltonian that captures all the essential symmetries and topology. On the other hand, it also introduces a short-distance cutoff so that the topological quantities can be well defined.

Within each 2 × 2 subblock, the Hamiltonian is of the general form studied in (*9*), in the context of the quantum anomalous Hall effect, where the Hall conductance is given by

$$\sigma_{xy} = -\frac{1}{8\pi^2}\iint dk_x dk_y \hat{\mathbf{d}} \cdot \partial_x \hat{\mathbf{d}} \times \partial_y \hat{\mathbf{d}} \quad (7)$$

in units of e^2/h (the square of the charge on the electron divided by the Planck constant), where $\hat{\mathbf{d}}$ denotes the unit $d_i(k)$ vector introduced in the Hamiltonian Eq. 2. When integrated over the full Brillouin zone, σ_{xy} is quantized to take integer values that measure the skyrmion number, or the number of times the unit $\hat{\mathbf{d}}$ winds around the unit sphere over the Brillouin zone torus. The topological structure can be best visualized by plotting $\hat{\mathbf{d}}$ as a function of k. In a skyrmion with a unit of topological charge, the $\hat{\mathbf{d}}$ vector points to the north (or the south) pole at the origin, points to the south (or the north) pole at the zone boundary, and winds around the equatorial plane in the middle region.

Substituting the continuum expression for the $d_i(k)$ vector as given in Eq. 3, and cutting off the integral at some finite point in momentum space, one obtains $\sigma_{xy} = {}^1/_2\ sign\ (M)$, which is a well-known result in field theory (*23*). In the continuum model, the $\hat{\mathbf{d}}$ vector takes the configuration of a meron, or half of a skyrmion, where it points to the north (or the south) pole at the origin and winds around the equator at the boundary. As the meron is half of a skyrmion, the integral Eq. 7 gives $\pm{}^1/_2$. The meron configuration of $d_i(k)$ is depicted in Fig. 2, B and C. In a noninteracting system, half-integral Hall conductance is not possible, which means that other points from the Brillouin zone must either cancel or add to this contribution so that the total Hall conductance becomes an integer. The fermion-doubled partner (*24*) of our low-energy fermion near the Γ point lies in the higher-energy spectrum of the lattice and contributes to the total σ_{xy}. Therefore, our effective Hamiltonian near the Γ point cannot yield a precise determination of the Hall conductance for the whole system. However, as one changes the quantum well thickness d across d_c, M changes sign and the gap closes at the Γ point, leading to a vanishing $d_i(k = 0)$ vector at the transition point $d = d_c$. The sign change of M leads to a well-defined change of the Hall conductance $\Delta\sigma_{xy} = 1$ across the transition. As the $d_i(k)$ vector is regular at the other parts of the Brillouin zone, these parts cannot lead to any discontinuous changes across the transition point at $d = d_c$.

So far, we have only discussed one 2 × 2 block of the effective Hamiltonian H. General time-reversal symmetry dictates that $\sigma_{xy}(H) = -\sigma_{xy}(H^*)$; therefore, the total charge Hall conductance vanishes, and the spin Hall conductance (given by the difference between the two blocks) is finite and given by $\Delta\sigma_{xy}^{(s)} = 2$ in units of e^2/h. From the general relationship between the quantized Hall conductance and the number of edge states (*25*), we conclude that the two sides of the phase transition at $d = d_c$ must differ in the number of pairs of helical edge states by 1, thus concluding our proof that one side of the transition must be Z_2 odd and topologically distinct from a fully gapped conventional insulator.

It is desirable to establish which side of the transition is topologically nontrivial. For this purpose, we return to the tight-binding model Eq. 6. The Hall conductance of this model has been calculated (*25*) in the context of the quantum anomalous Hall effect, and previously in the context of lattice fermion simulation (*26*). Besides the Γ point, which becomes gapless at $M/2B = 0$, there are three other high-symmetry points in the Brillouin zone. The (0,π) and (π,0) points become gapless at $M/2B = 2$, whereas the (π,π) point becomes gapless at $M/2B = 4$. Therefore, at $M/2B = 0$, there is only one gapless Dirac point per 2 × 2 block. This behavior is qualitatively different from the Haldane model of graphene (*27*), which has two gapless Dirac points in the Brillouin zone. For $M/2B < 0$, $\sigma_{xy} = 0$; for $0 < M/2B < 2$, $\sigma_{xy} = 1$. Because this condition is satisfied in the inverted gap regime where $M/2B = 2.02 \times 10^{-4}$ at 70 Å (*22*) and not in the normal regime where $M/2B < 0$, we believe that the inverted case is the topologically nontrivial regime supporting a QSH state.

We now discuss the experimental detection of the QSH state. A series of purely electrical measurements can be used to detect the basic signature of the QSH state. By sweeping the gate voltage, one can measure the two-terminal conductance G_{LR} from the p-doped to bulk-insulating to n-doped regime (Fig. 3). In the bulk insulating regime, G_{LR} should vanish at low temperatures for a normal insulator at $d < d_c$, whereas G_{LR} should approach a value close to $2e^2/h$ for $d > d_c$. Strikingly, in a six-terminal measurement, the QSH state would exhibit vanishing electric voltage drop between the terminals μ_1 and μ_2 and between μ_3 and μ_4, in the zero temperature limit and in the presence of a finite electric current between the L and R terminals. In other words, longitudinal resistance should vanish in the zero temperature limit, with a power-law dependence, over distances larger than the mean free path. Because of the absence of backscattering, and before spontaneous breaking of time reversal sets in, the helical edge currents flow without dissipation, and the voltage drop occurs only at the drain side of the contact (*11*). The vanishing of the longitudinal resistance is one of the most remarkable manifestations of the QSH state. Finally, a spin-filtered measurement can be used to determine the spin Hall conductance $\sigma_{xy}^{(s)}$. Numerical calculations (*13*) show that it should take a value close to $\sigma_{xy}^{(s)} = 2e^2/h$.

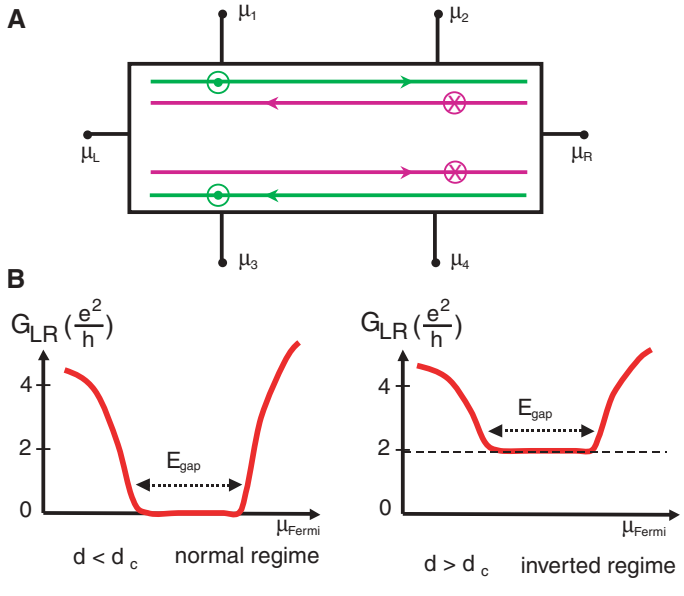

Fig. 3. (**A**) Experimental setup on a six-terminal Hall bar showing pairs of edge states, with spin-up states in green and spin-down states in purple. (**B**) A two-terminal measurement on a Hall bar would give G_{LR} close to $2e^2/h$ contact conductance on the QSH side of the transition and zero on the insulating side. In a six-terminal measurement, the longitudinal voltage drops $\mu_2 - \mu_1$ and $\mu_4 - \mu_3$ vanish on the QSH side with a power law as the zero temperature limit is approached. The spin Hall conductance $\sigma_{xy}^{(s)}$ has a plateau with the value close to $2e^2/h$.

Constant experimental progress on HgTe over the past two decades makes the experimental realization of our proposal possible. The mobility of the HgTe-CdTe quantum wells has reached $\mu \sim 6 \times 10^5$ cm^2 V^{-1} s^{-1} (*28*). Experiments have already confirmed the different characters of the upper band below ($E1$) and above ($H1$) the critical thickness d_c (*20*, *29*). The experimental results are in excellent agreement with band-structure calculations based on $k \cdot p$ theory. Our proposed two-terminal and six-terminal electrical measurements can be carried out on existing samples without radical modification, with samples of $d < d_c \approx 64$ Å and $d > d_c \approx 64$ Å yielding contrasting results. As a consequence, we believe that the experimental detection of the QSH state in HgTe-CdTe quantum wells is possible.

References and Notes

1. M. I. Dyakonov, V. I. Perel, *Phys. Lett. A* **35**, 459 (1971).
2. S. Murakami, N. Nagaosa, S. C. Zhang, *Science* **301**, 1348 (2003).
3. J. Sinova *et al.*, *Phys. Rev. Lett.* **92**, 126603 (2004).
4. Y. Kato *et al.*, *Science* **306**, 1910 (2004).
5. J. Wunderlich, B. Kaestner, J. Sinova, T. Jungwirth, *Phys. Rev. Lett.* **94**, 047204 (2005).
6. S. Murakami, N. Nagaosa, S. C. Zhang, *Phys. Rev. Lett.* **93**, 156804 (2004).
7. C. L. Kane, E. J. Mele, *Phys. Rev. Lett.* **95**, 226801 (2005).
8. B. A. Bernevig, S. C. Zhang, *Phys. Rev. Lett.* **96**, 106802 (2006).
9. X.-L. Qi, Y. S. Wu, S. C. Zhang, *Phys. Rev. B* **74**, 085308 (2006).
10. C. L. Kane, E. J. Mele, *Phys. Rev. Lett.* **95**, 146802 (2005).
11. C. Wu, B. A. Bernevig, S. C. Zhang, *Phys. Rev. Lett.* **96**, 106401 (2006).
12. C. Xu, J. Moore, *Phys. Rev. B* **73**, 045322 (2006).
13. L. Sheng *et al.*, *Phys. Rev. Lett.* **95**, 136602 (2005).
14. M. Onoda, Y. Avishai, N. Nagaosa, http://arxiv.org/abs/cond-mat/0605510.
15. D. J. Thouless, M. Kohmoto, M. P. Nightingale, M. den Nijs, *Phys. Rev. Lett.* **49**, 405 (1982).
16. Y. Yao, F. Ye, X. L. Qi, S. C. Zhang, Z. Fang, http://arxiv.org/abs/cond-mat/0606350.
17. H. Min *et al.*, *Phys. Rev. B* **74**, 165310 (2006).
18. S. Murakami, http://arxiv.org/abs/cond-mat/0607001.
19. E. O. Kane, *J. Phys. Chem. Solids* **1**, 249 (1957).
20. E. G. Novik *et al.*, *Phys. Rev. B* **72**, 035321 (2005).
21. A. Pfeuffer-Jeschke, thesis, University of Würzburg (2000).
22. See supporting material on *Science* Online.
23. A. N. Redlich, *Phys. Rev. D* **29**, 2366 (1984).
24. H. B. Nielsen, M. Ninomiya, *Nucl. Phys. B* **185**, 20 (1981).
25. X. L. Qi, Y. S. Wu, S. C. Zhang, *Phys. Rev. B* **74**, 045125 (2006).
26. M. F. L. Golterman, K. Jansen, D. B. Kaplan, *Phys. Lett. B* **301**, 219 (1993).
27. F. D. M. Haldane, *Phys. Rev. Lett.* **60**, 635 (1988).
28. K. Ortner *et al.*, *Appl. Phys. Lett.* **79**, 3980 (2001).
29. C. R. Becker, V. Latussek, A. Pfeuffer-Jeschke, G. Landwehr, L. W. Molenkamp, *Phys. Rev. B* **62**, 10353 (2000).

30. We thank X. Dai, Z. Fang, F. D. M. Haldane, A. H. MacDonald, L. W. Molenkamp, N. Nagaosa, X.-L. Qi, R. Roy, and R. Winkler for discussions. B.A.B. acknowledges the hospitality of the Kavli Institute for Theoretical Physics at the University of California, Santa Barbara, where part of this work was performed. Supported by NSF grant DMR-0342832 and by the U.S. Department of Energy, Office of Basic Energy Sciences, under contract DE-AC03-76SF00515.

Supporting Online Material

www.sciencemag.org/cgi/content/full/314/5806/1757/DC1
SOM Text
Fig. S1
Table S1
References

10 August 2006; accepted 1 November 2006
10.1126/science.1133734

Photoconductive Coaxial Nanotubes of Molecularly Connected Electron Donor and Acceptor Layers

Yohei Yamamoto,[1] Takanori Fukushima,[1,2]* Yuki Suna,[1] Noriyuki Ishii,[3] Akinori Saeki,[4] Shu Seki,[4] Seiichi Tagawa,[4] Masateru Taniguchi,[4] Tomoji Kawai,[4] Takuzo Aida[1,2]*

Controlled self-assembly of a trinitrofluorenone-appended gemini-shaped amphiphilic hexabenzocoronene selectively formed nanotubes or microfibers with different photochemical properties. In these nanotubes, which are 16 nanometers in diameter and several micrometers long, a molecular layer of electron-accepting trinitrofluorenone laminates an electron-donating graphitic layer of π-stacked hexabenzocoronene. The coaxial nanotubular structure allows photochemical generation of spatially separated charge carriers and a quick photoconductive response with a large on/off ratio greater than 10^4. In sharp contrast, the microfibers consist of a charge-transfer complex between the hexabenzocoronene and trinitrofluorenone parts and exhibit almost no photocurrent generation.

As exemplified by organic photovoltaic devices (*1*–*3*), heterojunction of electron donor and acceptor layers at a macroscopic level allows for the conversion of light energy into electrical energy (*4*, *5*). If one can elaborate a nano-object composed of molecularly conjugated domains of such a redox couple, the resultant material is expected to serve as a nanoscopic energy converter. However, donor and acceptor molecules tend to stack on one another, rather than segregate (*6*–*8*), giving rise to charge-transfer (CT) assemblies (*9*–*11*), in which photochemically generated charge carriers are trapped and readily annihilated through a rapid recombination. Here we report a coaxial nanotubular object formed by controlled self-assembly of trinitrofluorenone (TNF)–appended hexabenzocoronene (HBC) amphiphile **1** (Fig. 1A), in which a molecular layer of electron-accepting TNF laminates an electron-donating graphitic layer of π-stacked HBC (Fig. 2) (*12*). This structure creates an extremely wide interface for the spatially segregated redox couple so that, upon photoirradiation, the electrical conduction has a large on/off ratio (>10^4) that is difficult to attain with other carbon-based materials (*13*–*15*). Such molecularly engineered photoconductive materials with a tubular morphology are unusual and join the few examples of photoconductive nanostructured assemblies that have been reported (*7*, *16*).

HBC derivatives with symmetrically substituted paraffinic side chains form discotic liquid-crystalline materials that exhibit a hole-transport capability through their one-dimensional columnar HBC stacks (*5*, *17*–*21*). Recently, we have discovered that gemini-shaped amphiphilic HBCs (structure **3**, Fig. 1A) can self-assemble to form well-defined nanotubular objects, whose walls consist of a graphitic layer of π-stacked HBC and whose inner and outer surfaces are covered by hydrophilic triethylene glycol (TEG) chains (*22*, *23*). Upon doping with oxidants, the HBC graphitic nanotubes become electrically conductive (*22*, *24*). In the present work, we prepared HBC-TNF **1** and **2**, which bear an electron-accepting 4,5,7-trinitro-9-fluorenone functionality (*25*) at each terminus of either (**1**) and both (**2**) of the TEG chains (Fig. 1A). The energy levels of the highest occupied molecular orbital (HOMO) and the lowest unoccupied molecular orbital (LUMO) of HBC **3** (*22*) and TNF **4** (*26*) (Fig. 1B) were determined by means of square-wave voltammetry and electronic absorption spectroscopy (fig. S1) (*27*). Apparently, photoinduced electron transfer is energetically possible between the HBC and TNF functionalities of **1** and **2**.

Compounds **1** and **2** were synthesized by oxidative cyclization of the corresponding hexaphenylbenzene precursors with $FeCl_3$ in CH_2Cl_2/$MeNO_2$ (*27*). Both compounds in tetrahydrofuran (THF) were colored brown, indicating a CT interaction between the HBC and TNF parts in

[1]Aida Nanospace Project, Exploratory Research for Advanced Technology–Solution Oriented Research for Science and Technology (ERATO-SORST), Japan Science and Technology Agency, National Museum of Emerging Science and Innovation, 2-41 Aomi, Koto-ku, Tokyo 135–0064, Japan. [2]Department of Chemistry and Biotechnology, School of Engineering, and Center for NanoBio Integration, The University of Tokyo, 7-3-1 Hongo, Bunkyo-ku, Tokyo 113–8656, Japan. [3]Biological Information Research Center, National Institute of Advanced Industrial Science and Technology, Tsukuba Central-6, 1-1-1 Higashi, Tsukuba, Ibaraki 305–8566, Japan. [4]Institute of Scientific and Industrial Research, Osaka University, 8-1 Mihogaoka, Ibaraki, Osaka 567–0047, Japan.

*To whom correspondence should be addressed. E-mail: fukushima@nanospace.miraikan.jst.go.jp (T.F.); aida@macro.t.u-tokyo.ac.jp (T.A.)